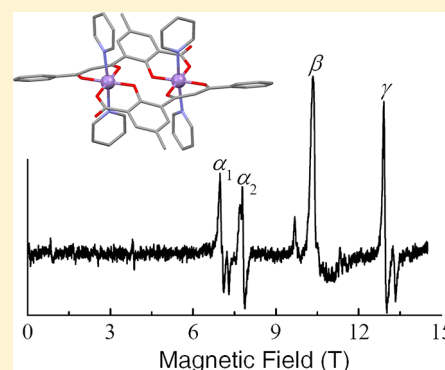


Elucidating Magnetic Exchange and Anisotropy in Weakly Coupled Mn^{III} DimersJunjie Liu,^{†,‡} J. Krzystek,[‡] Stephen Hill,^{*,‡,§} Leoní Barrios,^{||} and Guillem Aromí^{*,||}[†]Department of Physics, University of Florida, Gainesville, Florida 32301, United States[‡]National High Magnetic Field Laboratory and [§]Department of Physics, Florida State University, Tallahassee, Florida 32310, United States^{||}Departament de Química Inorgànica, Universitat de Barcelona, 08028 Barcelona, Spain

ABSTRACT: High-frequency Electron Paramagnetic Resonance (HF-EPR) measurements have been performed on both a single-crystal and powder samples of a weakly coupled antiferromagnetic dinuclear [Mn^{III}]₂ molecular magnet, [Mn^{III}₂L₂(py)₄], where L is the trianion of 3-(3-oxo-3-phenylpropionyl)-5-methylsalicylic acid, and py is pyridine. The experimental results were analyzed on the basis of a multispin Hamiltonian using both a perturbative approach and numerical simulations. It is found that the single-crystal HF-EPR results provide a direct and simple means of determining both the axial anisotropy of the individual Mn^{III} ions and the isotropic exchange coupling between them. Previously unpublished low-temperature magnetization data are then simulated using the same model Hamiltonian, yielding excellent agreement. This work highlights the limitations of widely used protocols for analyzing magnetic and powder EPR data obtained for multinuclear molecular magnets in which the exchange and single-ion anisotropies are comparable, thus emphasizing the value of single-crystal, multifrequency EPR measurements.



■ INTRODUCTION

Polynuclear transition metal clusters attract considerable interest in the inorganic and bioinorganic research communities because of their interesting magnetic properties and their relevance to important catalytic/enzymatic processes in nature.^{1–8} Understanding the magnetic properties of transition metal clusters depends on resolving the interactions between the constituent metal ions comprising their cores. While large molecules are attractive because of the possibility of achieving sizable magnetic moments and associated magneto-anisotropies, which are important for many potential applications, their complexity often obscures important underlying physics. A common protocol for understanding the low temperature physics of a polynuclear cluster involves treating its total spin as an exact quantum number, that is, one ignores the internal molecular degrees of freedom by essentially assuming that the exchange interactions within the molecule are infinite so that it behaves as a rigid, giant-spin.⁹ However, such an approximation does not work for molecules in which the exchange interactions between metal centers are of the same order (or smaller) as the local magneto-anisotropies associated with the constituent ions. In this weak exchange regime, one can no longer apply the macro-spin phenomenology. Moreover, one cannot neglect the magneto-anisotropy when analyzing temperature-dependent thermodynamic measurements. One is thus forced to invoke a multispin description that takes into account both the local anisotropy tensors of the constituent ions and the exchange coupling between them for analysis of all magnetic and EPR

data.¹⁰ However, this approach can be computationally challenging for large/complex clusters.

To gain further insights into the weak exchange regime, particularly with regards to fitting of magnetic data,¹¹ it is helpful to study simple molecules consisting of just a few metal centers.⁵ However, the presence of multiple, inequivalent interaction pathways (with different exchange constants) within polynuclear molecules makes it difficult to constrain these interactions unambiguously. In most studies, certain levels of approximation are required to eliminate the number of free parameters involved in fitting magnetometric data, for example, by assuming the same interaction for all (or several) of the exchange pathways.^{12,13} However, such simplifications invariably result in a spin Hamiltonian that has a higher symmetry than the actual molecule. Even dinuclear molecules—the simplest platforms for studying the interplay between anisotropy and exchange—often require an intimidating level of theory and spectroscopic measurements,^{14–17} particularly when non-Heisenberg spin-spin interactions are necessary to interpret spectroscopic measurements.^{16–18} Since the most prevalent metal ion occurring in molecular magnetism is Mn^{III}, we have synthesized and grown single crystals of a dimeric complex abbreviated as [Mn^{III}₂L₂(py)₄] (**1**),¹⁹ where L is the trianion of 3-(3-oxo-3-phenylpropionyl)-5-methylsalicylic acid, and py is pyridine, to

Received: August 23, 2012

Published: December 28, 2012

study the effects of the weak exchange between the two Mn^{III} ions.

The structure and magnetic susceptibility of **1** have been reported previously.¹⁹ In this article we present extensive High-Frequency Electron Paramagnetic Resonance (HFEP) measurements on **1**, which is also a candidate material for investigating the magnetic properties of molecular magnets under pressure.²⁰ The objective of the present work is 2-fold: in the first place, we show that the low-temperature HFEP results can be understood semianalytically by solving a multispin Hamiltonian which includes only the second order single-ion anisotropy and a Heisenberg exchange interaction. In the second place, based on the parameters obtained via EPR studies, we explain previous magnetization measurements that were not understood in the earlier studies. Our model quantitatively reproduces a non-monotonic behavior of the isofield magnetization curves, which is not possible using more widely employed approximate methods based on the giant-spin approach.

EXPERIMENTAL SECTION

The crystal structure of [Mn₂L₂(py)₄], as reported in ref 19, is shown in Figure 1. The Mn^{III} ions in the molecule are six-coordinate in a Jahn–

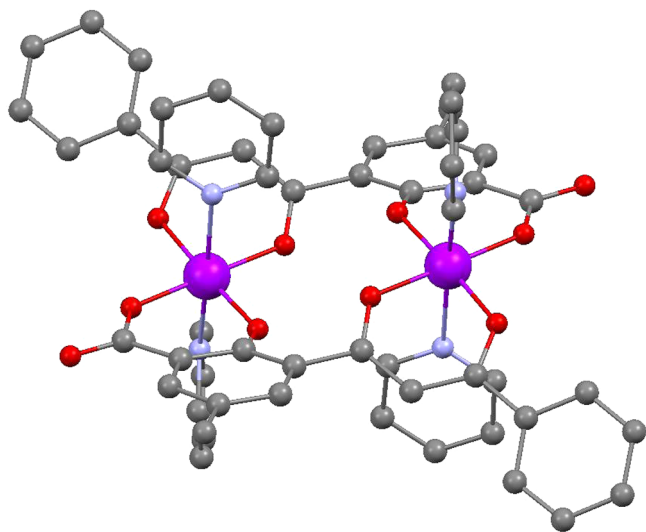


Figure 1. Molecular structure of complex **1**. Color code: Mn = purple, O = red, N = blue, and C = gray. H-atoms have been omitted for clarity.

Teller (JT) elongated octahedral geometry, with the JT axes defined by the Mn–N bonds. The distance between the two Mn^{III} ions in the molecule is 5.261 Å, with the shortest contacts connecting the two Mn^{III} ions being the –O–C–C–C–O– bonds. The molecule crystallizes in the triclinic space group $P\bar{1}$, and it sits on an inversion center. Consequently, the JT axes associated with the two Mn^{III} ions are parallel.

Magnetic measurements (susceptibility vs temperature, and magnetization vs field) were performed on a Quantum Design MPMS-SS SQUID magnetometer. HFEP measurements were carried out at the National High Magnetic Field Laboratory, in Tallahassee, Florida, on both single crystals and powder samples of **1**. Single crystal measurements were performed in a 7 T horizontal-bore, split-gap superconducting magnet with temperature control achieved using a ⁴He flow cryostat. A Millimeter-wave Vector Network Analyzer served as a microwave source and detector, and a cavity perturbation technique was employed to measure a very small, needle-shaped single crystal with approximate dimensions 150 × 150 × 500 μm.^{21,22} Powder HFEP measurements were carried out in a transmission-type spectrometer based on a 15 T superconducting magnet. A phase-locked oscillator, in conjunction with a series of multipliers and amplifiers, was employed as a

microwave source capable of providing quasi-continuous frequency coverage up to 600+ GHz; a cold bolometer was used for detection.²³ The sample was finely ground and restrained by *n*-eicosane in a Teflon container.

RESULTS AND DISCUSSION

HFEP. We started with experiments on a powdered sample of **1**, with an example of an EPR spectrum shown in the main panel of Figure 2. The sample produced a very strong and well-

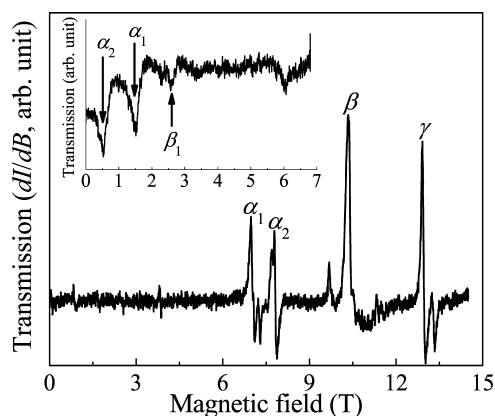


Figure 2. Powder EPR spectrum for complex **1** obtained at 652.8 GHz and 10 K (recorded in the first-derivative mode). The EPR transitions have been labeled according to their behavior in the frequency dependence studies (see detailed discussion in the main text). The inset displays a single-crystal spectrum for complex **1**, obtained at 418 GHz and 2 K (recorded in absorption mode), with the orientation of the field being close to the molecular *z*-axis. Note that this single crystal spectrum was collected with a frequency below the ZFS which results in the order of α_1 and α_2 being reversed compared with the high frequency spectrum (see Figure 3).

defined EPR response over the entire available frequency range. However, this rich spectrum was essentially uninterpretable. Qualitatively, it shows that the interactions between the Mn^{III} ions create new spin states that are unlike those of the individual ions, as the spectrum does not resemble that of a single Mn^{III} ion ($S = 2$ system). At the same time, we did not succeed in interpreting the results in terms of a well-defined giant spin state. We thus performed HFEP measurements on a single crystal to quantitatively determine the magnetic properties of the molecule.

An example of a single-crystal spectrum is shown in the inset of Figure 2. Single axis crystal rotation was carried out first to align the externally applied field close to the molecular easy (*z*-) axis. Following that, extensive frequency and temperature dependence studies (380–510 GHz, 2–20 K) were performed at this fixed orientation. Figure 3a shows the peak positions of the observed EPR transitions in a crystal for $B_0 \parallel z$ at 2 K. Temperature-dependent measurements (not shown) confirmed that the two transition branches observed at low fields, which are labeled α_1 and α_2 in Figure 3a, originate from the ground spin state.

Since we could not use the giant-spin approximation to analyze the data, because the ground spin state is not well-defined, a more physical model was proposed using the following Hamiltonian:

$$\hat{H} = d\hat{s}_{z1}^2 + d\hat{s}_{z2}^2 + J\hat{s}_1 \cdot \hat{s}_2 + \mu_B \vec{B}_0 \cdot \vec{g} \cdot (\hat{s}_1 + \hat{s}_2) \quad (1)$$

The first two terms represent the single-ion anisotropies of the individual Mn^{III} ions, where d is the second order axial anisotropy

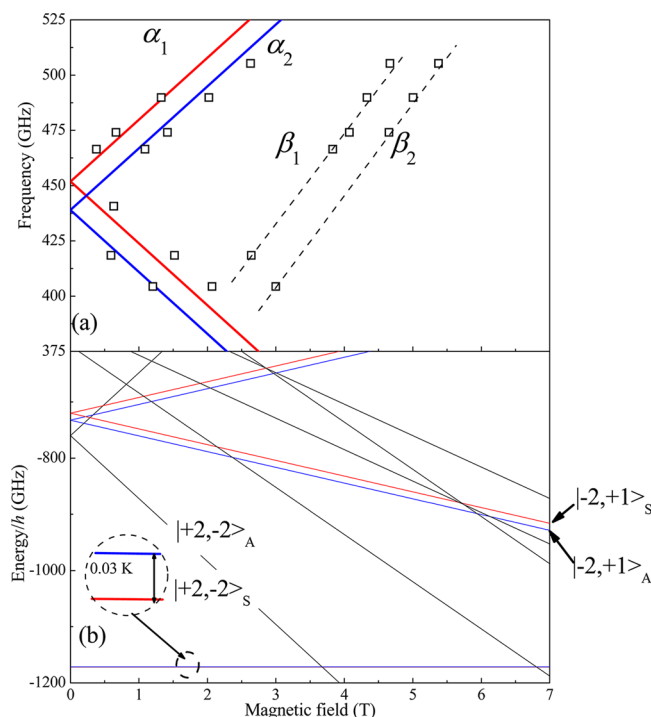


Figure 3. Single-crystal EPR studies for complex **1**. (a) Frequency versus field plot showing the EPR peak positions for a single crystal with the field applied close to the molecular *z*-axis at 2 K. The squares are the experimental data while the solid lines are simulations of the EPR peak positions. The dashed lines are guides to the eyes. The simulations were performed with the Hamiltonian and parameters discussed in the main text. (b) Simulated energy level diagram. The parities of the states are indicated by color, where red is even (symmetric) and blue is odd (antisymmetric). The 0th-order eigenvectors of the states associated with α transitions are labeled in the figure.

constant. We chose the same d value for both Mn^{III} ions, as required by the inversion symmetry of the molecule. The third term corresponds to the Heisenberg interaction, with J parametrizing the isotropic exchange coupling between the two Mn^{III} ions. The last term is the Zeeman coupling to the applied field, where we assume an isotropic Landé g factor, $g = 2.00$, which is typical for Mn^{III} . Equation 1 is the simplest Hamiltonian that one can use to describe complex **1**. Moreover, in spite of several simplifying assumptions, such as neglecting transverse (rhombic) single-ion anisotropy, it can explain the two key experimental results very well, that is, the HF-EPR spectra and the magnetic data.

Before presenting a detailed analysis of the HF-EPR spectra, we should discuss the EPR selection rules that are applicable in this case. Because **1** does not possess well-defined spin states, one cannot apply the normal selection rules, $\Delta S = 0$ and $\Delta m = \pm 1$. However, since only axial anisotropy is included in eq 1, m remains a good quantum number when the field is applied along the molecular *z*-axis. Thus, the selection rule $\Delta m = \pm 1$ still holds. Furthermore, because of the inversion symmetry of the molecule, all eigenvectors must have a definite parity upon exchanging two spins, that is, symmetric (even) or antisymmetric (odd). The magnetic-dipole (EPR) transition probability is nonzero only if the transition occurs between states having the same parity. Therefore, we conclude that the EPR selection rules for **1** are (a) $\Delta m = \pm 1$; and (b) the parity of the initial and final states must be conserved.

Figure 3b shows the low energy part of the simulated Zeeman diagram of **1** with the field applied along the molecular *z*-axis. This simulation was performed employing eq 1 with the following parameters: $d = -5.76$ K and $J = +2.45$ K. These parameters give good agreement for both single-crystal and powder EPR results (vide infra). The obtained anisotropy parameter is similar to that reported for a closely related monomeric Mn^{III} species.²⁴ To understand the origin of the observed EPR transitions, one needs to consider the symmetry of the eigenvectors corresponding to the energy levels in Figure 3b. To do this, we treat the diagonal part of eq 1, $d\hat{s}_{z1}^2 + d\hat{s}_{z2}^2 + J\hat{s}_{z1}\hat{s}_{z2} + g\mu_{\text{B}}B_0(\hat{s}_{z1} + \hat{s}_{z2})$, as the unperturbed Hamiltonian, \hat{H}_0 , and the off-diagonal part of the Heisenberg interaction, $1/2 J(\hat{s}_1^+\hat{s}_2^- + \hat{s}_1^-\hat{s}_2^+)$, as a perturbation, \hat{H}' , where \hat{s}_i^{\pm} are the spin-ladder operators and $\hat{H} = \hat{H}_0 + \hat{H}'$. As we will show, this perturbative treatment gives both quantitative agreement, and an intuitive picture of the experimental results.

If $J = 0$, the molecule is composed of two noninteracting spins; hence, the eigenvectors of the molecule can be written as direct products of the uncoupled Mn^{III} eigenvectors, $|m_1\rangle$ and $|m_2\rangle$ (abbreviated as $|m_1, m_2\rangle$), where m_1 and m_2 represent the spin projections of the individual Mn^{III} ions onto the molecular *z*-axis, and $m = m_1 + m_2$. At zero field, the ground state of the molecule is quadruply degenerate, where the four states can be denoted: $|+2, +2\rangle$, $|+2, -2\rangle$, $|-2, +2\rangle$, and $|-2, -2\rangle$. These correspond to two uncoupled spins, where the eigenvectors are not constrained by parity. When we include a small antiferromagnetic interaction, the eigenvectors should be written as the symmetric/antisymmetric superpositions of these states in order that they have definite parities. Thus, the eigenvectors for the four ground states are: $|+2, +2\rangle$ ($m = +4$), $|-2, -2\rangle$ ($m = -4$), $2^{-1/2}(|+2, -2\rangle + |-2, +2\rangle)$ ($m = 0$), and $2^{-1/2}(|+2, -2\rangle - |-2, +2\rangle)$ ($m = 0$). For the sake of simplicity, we abbreviate $2^{-1/2}(|m_a, m_b\rangle + |m_b, m_a\rangle)$ as $|m_a, m_b\rangle_{\text{S}}$ and $2^{-1/2}(|m_a, m_b\rangle - |m_b, m_a\rangle)$ as $|m_a, m_b\rangle_{\text{A}}$ ($m_a \neq m_b$) where the subscript S (symmetric) and A (antisymmetric) denotes the parity of the superposition states. We then deduce the zero-field eigen-energies in the absence of the perturbation, \hat{H}' . As expected, the exchange coupling lifts the degeneracy of the $m = 0$ and ± 4 states, such that

$$\begin{aligned} \langle +2, -2 | \hat{H}_0 | +2, -2 \rangle_{\text{A}} &= \langle +2, -2 | \hat{H}_0 | +2, -2 \rangle_{\text{S}} = 8d - 4J \\ \langle +2, +2 | \hat{H}_0 | +2, +2 \rangle &= \langle -2, -2 | \hat{H}_0 | -2, -2 \rangle = 8d + 4J \end{aligned} \quad (2)$$

The inclusion of J splits the $m = 0$ states from the $m = \pm 4$ states by $8J$. Because the interaction is antiferromagnetic ($J > 0$), the zero-field ground states of the molecule are now the nonmagnetic ($m = 0$) $|+2, -2\rangle_{\text{A}}$ and $|-2, +2\rangle_{\text{S}}$ states, as seen in Figure 3b. The small energy difference between these states originates from higher-order perturbation corrections involving \hat{H}' , which we discuss further below.

Now we consider the origin of the α_1 and α_2 transitions observed in single-crystal EPR measurements. According to the preceding discussion, the ground states are two $m = 0$ levels. Therefore, the final states associated with the α_1 and α_2 transitions must be $m = \pm 1$ states. For the sake of simplicity, we only consider the $m = -1$ states in our analysis. When $J = 0$, the eigenvectors associated with the possible $m = -1$ states are $|-2, 1\rangle$, $|1, -2\rangle$, $|-1, 0\rangle$, and $|0, -1\rangle$, where $|-2, 1\rangle$ and $|1, -2\rangle$ are considerably lower in energy because of the strong uniaxial anisotropy. Upon including a small exchange interaction, the eigenvectors of these states become $|-2, +1\rangle_{\text{A}}$ and $|-2, +1\rangle_{\text{S}}$. Their unperturbed energies are then given by

$$\langle -2, +1 | \hat{H}_0 | -2, +1 \rangle_A = \langle -2, +1 | \hat{H}_0 | -2, +1 \rangle_S = 5d - 2J \quad (3)$$

It is important to point out that, when considering only the unperturbed Hamiltonian \hat{H}_0 , $|+2, -2\rangle_S$ and $|+2, -2\rangle_A$ are degenerate, and the two excited states, $|-2, +1\rangle_S$ and $|-2, +1\rangle_A$, are also degenerate. Hence, the EPR transition frequency/field associated with the symmetric states, $|+2, -2\rangle_S$ to $|-2, +1\rangle_S$, should be exactly the same as the one between the antisymmetric states, $|+2, -2\rangle_A$ to $|-2, +1\rangle_A$, which suggests only one ground EPR transition should be observed. The zero-field splitting (ZFS) associated with this transition, given by eqs 2 and 3, equals $| -3d + 2J | = 22.2$ K (or 462 GHz) according to the employed parameters. The ZFS values measured for the α_1 and α_2 branches are 451 and 438 GHz, respectively, which are in close agreement with this prediction.

To reproduce the splitting between α_1 and α_2 , one must consider the perturbation \hat{H}' , or solve eq 1 exactly via full matrix diagonalization. In the perturbation calculations, \hat{H}' mixes states with the same parity and m value, resulting in further corrections to the eigenvectors. For instance, the eigenvector of the symmetric $m = 0$ ground state is composed of linear combinations of $|2, -2\rangle_S$, $|1, -1\rangle_S$, and $|0, 0\rangle$, while the eigenvector of the antisymmetric $m = 0$ state is composed of linear combinations of $|2, -2\rangle_A$ and $|1, -1\rangle_A$. These corrections lift the degeneracy within the ground state. Simulations indicate that the energies of $|+2, -2\rangle_S$ and $|+2, -2\rangle_A$ differ by only 0.03 K (they are split by a very weak fourth-order degenerate perturbation), which means that both states have equal population in the experimental temperature range (≥ 2 K). However, this energy difference is too small to account for the observed splitting of the α_1 and α_2 resonances. However, the degeneracy of the $m = \pm 1$ states is also lifted by \hat{H}' , and it is the resulting energy splitting that accounts for the distinct α_1 and α_2 transitions. Since the perturbation depends only on the coupling constant J , one finds that the energy difference between the ZFS of the α_1 and α_2 resonances is approximately proportional to $|J|^3$ (the result of a third order perturbation).

Numerical simulations of the EPR transitions, employing eq 1 with $d = -5.76$ K and $J = +2.45$ K, are shown in Figure 3a. The two important parameters can be constrained purely on the basis of the α_1 and α_2 peak positions: the average ZFS of the two transitions is approximately equal to $| -3d + 2J |$, while the perturbation splitting between them provides a tight constraint on the interaction parameter J . We note that the obtained single-ion axial anisotropy of the Mn^{III} ions is similar to values reported in other octahedrally elongated coordination complexes,^{5,11,25} while the coupling constant J is consistent with the previous dc susceptibility measurements,¹⁹ albeit that those studies assumed an anisotropic interaction with $J_z = +3.14$ K and $J_x = J_y = 4$ K.

After obtaining the ZFS parameters from single-crystal studies, we returned to the powder spectra to see whether these parameters can explain the many other EPR transitions. Figure 4a shows peak positions collected from a powder sample at 10 K. The transitions are sorted into five different resonance branches, α_1 , α_2 , β , γ , and δ , on the basis of the peak positions of the high frequency data, as labeled in the figure. As shown, all of the resonance branches have roughly the same slope, corresponding to $g = 2.00$, $|\Delta m| = 1$ EPR transitions, which affirms the simplification of including only the axial anisotropy term. The solid lines in Figure 4a represent simulations of EPR peak positions, while Figure 4b shows the corresponding energy diagram. The field was applied parallel to the molecular z -axis in both cases. We also performed simulations (not shown) with the

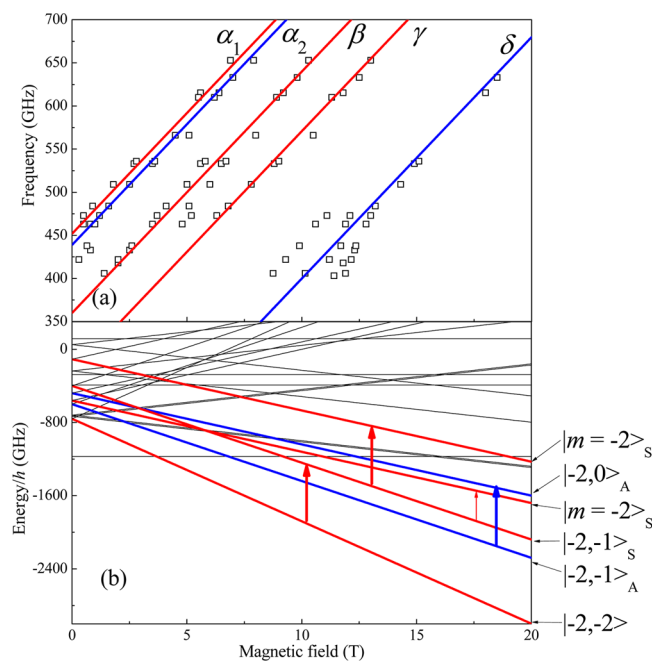


Figure 4. Powder EPR results for complex 1. (a) Frequency versus field plot showing the EPR peak positions at 10 K. The squares are experimental data while the solid lines are the simulated peak positions corresponding to the parallel (z -) components of the spectrum. (b) Simulation of the energy level diagram. The thick lines in (b) are the energy levels between which the strongest EPR transitions are observed. The states associated with the α transitions are ignored for clarity (see Figure 3). The states are color coded to denote their parities, where red stands for even (symmetric) and blue stands for odd (antisymmetric). The thick arrows in (b) represent the observed EPR transitions at approximately 650 GHz; the thin red arrow at ~ 17.5 T represents a weaker transition at a frequency of 300 GHz (650 GHz is out of the field range – see main text).

magnetic field applied in the molecular xy -plane, and the results indicate that the corresponding low-temperature EPR transitions all occur at fields above 15 T for the employed microwave frequencies; thus, they are not observed in these experiments. The low field branches, α_1 and α_2 , have been observed and discussed in the single-crystal studies. We focus here on the transitions occurring at high fields. The parities of the low energy states are colored either red (S) or blue (A) in Figure 4b, and the arrows indicate the observed EPR transitions at approximately 650 GHz. The final states of these transitions are determined by the EPR selection rules that were discussed previously: β corresponds to the $m = -4 \rightarrow -3$ transition between symmetric states, while γ and δ are the two $m = -3 \rightarrow -2$ transitions associated with symmetric and antisymmetric states, respectively. As shown in Figure 4b, all of the transitions are reasonably well explained by the aforementioned selection rules. We note that there are two symmetric $m = -2$ states. However, simulations reveal that the matrix element associated with the transition involving the higher-lying state (the thick red arrow) is more than 10 times stronger than that of the lower state (the thin red arrow). Furthermore, this transition occurs at fields above 20 T for the experimental frequencies employed (>400 GHz). Therefore, only the stronger transition is observed in the experiments.

Overall, the powder spectra are quite consistent with the single crystal studies and confirm the parameters deduced from single-crystal experiments, especially at the higher frequencies (see

Figure 4). However, some of the lower frequency transitions (below 550 GHz) cannot be explained so well, for example, the β_1 and β_2 resonances seen in the single crystal studies (Figure 2 and 3), and several others observed in the 400 to 450 GHz range in powder measurements. We suspect that this may be because we have oversimplified the Hamiltonian by neglecting transverse ZFS terms. Including a single-ion rhombic interaction, $e(\hat{S}_{xi}^2 - \hat{S}_{yi}^2)$, will lead to mixing between different m states, resulting in many additional EPR transitions. We also noticed that the simulations are extremely sensitive to the field orientation; once again, application of a transverse field mixes different m states, leading to additional EPR transitions, particularly at low-fields/frequencies. We thus speculate that the β_1 and β_2 transitions may emerge in single-crystal spectra when a small field misalignment is included, because perfect orientation of the crystal cannot be guaranteed. In contrast, powder measurements guarantee that the dominant features in the HFEP spectra correspond to the x , y , and z components of the ZFS tensor.

Magnetic Measurements. To validate the results obtained via HFEP measurements, we attempted to simulate the reduced magnetization (RM) results using the obtained parameters. The original RM measurements were performed in 2002. However, the result was never published because it could not be interpreted via any simple model, even when considering anisotropic exchange interactions.¹⁹ In magnetic measurements, if $|J| \gg |d|$, the high temperature regime is mostly affected by the energy difference between different S -multiplets (set by J), while low temperature measurements are mainly influenced by the ZFS (anisotropy) within the ground spin multiplet (determined by d). Therefore, the general strategy is to fit high temperature dc susceptibility ($\chi_m T$ vs T) measurements with an isotropic multispin Hamiltonian to obtain J , while low temperature RM data are fit to a giant-spin model to deduce d . However, as shown in our EPR analysis, d is two times larger than J for complex 1. If we consider an isotropic multispin model, the energy scale set by J is about $|8J|$, which corresponds to the energy difference between spins aligned parallel ($m = 4$) and antiparallel ($m = 0$). On the other hand, the zero-field splitting between the $|m_i = \pm 2\rangle$ and $|m_i = 0\rangle$ states for two Mn^{III} ions equals $|8d|$. Therefore, since d and J have similar magnitudes for 1, they will exert a comparable influence on the magnetic properties of 1 at all temperatures, thus highlighting the importance of including both the exchange and ZFS interactions in analyzing both $\chi_m T$ and RM data, that is, one must use eq 1 to fit the magnetic data.

The experimental and simulated RM results are shown in Figure 5. The squares are the experimental data, while the solid lines are the simulations employing eq 1 with the parameters obtained from the EPR studies. The experimental results show that, for a constant field, the magnetic moment of the sample goes through a maximum and then decreases upon reducing the temperature. The reduction of the magnetic moment at low temperatures can be understood in terms of the Zeeman diagram in Figure 4b, where the molecular ground states are nonmagnetic ($m = 0$) at fields below 3.7 T. Hence, the magnetic moment decreases at the lowest temperatures. Even at 4 T, the $m = 4$ state is very close in energy to the $m = 0$ states, which leads to a reduction of the magnetic moment at low temperatures, as seen for both the experiment and the simulations.

The simulations reproduce the main features of each iso-field curve in Figure 5, and give quantitative agreement for the 0.5 T, 1 T, and 2 T data. More importantly, the simulations exactly reproduce the positions of the maxima in the RM on the abscissa, which indicates that they correctly predict the temperatures at

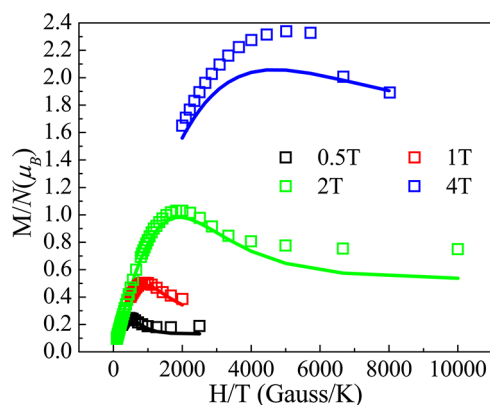


Figure 5. Plot of the iso-field reduced magnetization, M . The squares are experimental results while the solid lines are simulations employing the spin Hamiltonian and parameters provided in the main text.

which the magnetization saturates at different applied fields. The simulations confirm that the HFEP evaluation of the anisotropy and coupling between Mn^{III} ions is reliable, while small deviations in absolute value may come from the Landé- g factor not being exactly equal to 2 and/or experimental factors such as the samples being partially aligned by the magnetic field. From simulations we note that, below 3.7 T, the ground state of the molecule is nonmagnetic ($m = 0$) while, above 3.7 T, it is highly magnetic ($m = -4$). At low temperatures, when the field is above 3.7 T, a powder sample of 1 will experience a much stronger torque compared to lower fields. This may easily cause the sample to be partially aligned. We suspect that this might be the reason why the simulation and experimental data show a larger deviation at 4 T compared to the lower field results. Indeed, in the EPR experiments, strong hysteresis loops were observed when loose powders were used, presumably because of mechanical movement of microcrystals within the sample. The hysteresis vanished when the powder was constrained with *n*-eicosane.

CONCLUSIONS

Combined HFEP and static magnetic measurements quantitatively determined the magnetic properties of complex 1. Numerical simulations show that the combined data set may be explained very well by employing a spin Hamiltonian that parametrizes the Heisenberg coupling between two anisotropic $S = 2$ spins. This study provides important insights into the physics of molecular clusters that consist of weakly coupled metal ions. This work also demonstrates the usefulness of combining multiple techniques, as well as the limitations of employing standard magnetic data fitting procedures in the study of polynuclear systems characterized by weak exchange coupling. Finally, we note that complex 1 represents an ideal system in which to explore magnetostructural correlations as a function of hydrostatic pressure because both the exchange and the anisotropy parameters are easily extracted from the energies of just two strong ground state transitions, α_1 and α_2 .

AUTHOR INFORMATION

Corresponding Author

*E-mail: shill@magnet.fsu.edu (S.H.), guillem.aroni@qi.ub.es (G.A.).

Notes

The authors declare no competing financial interest.

ACKNOWLEDGMENTS

HFEPR studies were carried out at the National High Magnetic Field Laboratory, which is funded by the NSF through Cooperative Agreement DMR0654118, the State of Florida, and the U.S. Department of Energy. S.H. acknowledges the support of the NSF (Grant CHE0924374). G.A. thanks the Generalitat de Catalunya for the prize ICREA Academia 2008 for excellence in university research. L.B. and G.A. acknowledge the Spanish MCI for Grant CTQ2009-06959.

REFERENCES

- (1) Thomas, L.; Lioni, F.; Ballou, R.; Gatteschi, D.; Sessoli, R.; Barbara, B. *Nature* **1996**, *383*, 145.
- (2) Wernsdorfer, W.; Aliaga-Alcalde, N.; Hendrickson, D. N.; Christou, G. *Nature* **2002**, *416*, 406.
- (3) Hill, S.; Edwards, R. S.; Aliaga-Alcalde, N.; Christou, G. *Science* **2003**, *302*, 1015.
- (4) Ramsey, C. M.; del Barco, E.; Hill, S.; Shah, S. J.; Beedle, C. C.; Hendrickson, D. N. *Nat. Phys.* **2008**, *4*, 277.
- (5) Hill, S.; Datta, S.; Liu, J.; Inglis, R.; Milios, C. J.; Feng, P. L.; Henderson, J. J.; del Barco, E.; Brechin, E. K.; Hendrickson, D. N. *Dalton Trans.* **2010**, *39*, 4693.
- (6) Maayan, G.; Christou, G. *Inorg. Chem.* **2011**, *50*, 7015.
- (7) Artero, V.; Chavarot-Kerlidou, M.; Fontecave, M. *Angew. Chem., Int. Ed.* **2011**, *50*, 7238.
- (8) McAlpin, J. G.; Stich, T. A.; Ohlin, C. A.; Surendranath, Y.; Nocera, D. G.; Casey, W. H.; Britt, R. D. *J. Am. Chem. Soc.* **2011**, *133*, 15444.
- (9) Gatteschi, D.; Sessoli, R.; Villain, J. *Molecular Nanomagnets*; Oxford University Press: Oxford, U.K., 2006.
- (10) Liu, J.; Koo, C.; Amjad, A.; Feng, P. L.; Choi, E. S.; del Barco, E.; Hendrickson, D. N.; Hill, S. *Phys. Rev. B* **2011**, *84*, 094443.
- (11) Inglis, R.; Houton, E.; Liu, J.; Prescimone, A.; Cano, J.; Piligkos, S.; Hill, S.; Jones, L. F.; Brechin, E. K. *Dalton Trans.* **2011**, *40*, 9999.
- (12) Accorsi, S.; Barra, A.-L.; Caneschi, A.; Chastanet, G.; Cornia, A.; Fabretti, A. C.; Gatteschi, D.; Mortalò, C.; Olivieri, E.; Parenti, F.; Rosa, P.; Sessoli, R.; Sorace, L.; Wernsdorfer, W.; Zobbi, L. *J. Am. Chem. Soc.* **2006**, *128*, 4742.
- (13) van Slageren, J.; Piligkos, S.; Neese, F. *Dalton Trans.* **2010**, *39*, 4999.
- (14) Maurice, R.; Guihéry, N.; Bastardis, R.; de Graaf, C. *J. Chem. Theory Comput.* **2009**, *6*, 55.
- (15) Maurice, R.; de Grcutaaf, C.; Guihéry, N. *Phys. Rev. B* **2010**, *81*, 214427.
- (16) Semenaka, V. V.; Nesterova, O. V.; Kokozay, V. N.; Dyakonenko, V. V.; Zubatyuk, R. I.; Shishkin, O. V.; Boča, R.; Jezierska, J.; Ozarowski, A. *Inorg. Chem.* **2010**, *49*, 5460.
- (17) Boeer, A. B.; Barra, A.-L.; Chibotaru, L. F.; Collison, D.; McInnes, E. J. L.; Mole, R. A.; Simeoni, G. G.; Timco, G. A.; Ungur, L.; Unruh, T.; Winpenny, R. E. P. *Angew. Chem., Int. Ed.* **2011**, *50*, 4007.
- (18) Herchel, R.; Boča, R.; Krzystek, J.; Ozarowski, A.; Durán, M.; van Slageren, J. *J. Am. Chem. Soc.* **2007**, *129*, 10306.
- (19) Aromí, G.; Gamez, P.; Roubeau, O.; Berzal, P. C.; Kooijman, H.; Spek, A. L.; Driessen, W. L.; Reedijk, J. *Inorg. Chem.* **2002**, *41*, 3673.
- (20) Prescimone, A.; Morien, C.; Allan, D.; Schlueter, J. A.; Tozer, S. W.; Manson, J. L.; Parsons, S.; Brechin, E. K.; Hill, S. *Angew. Chem., Int. Ed.* **2012**, *51*, 7490.
- (21) Mola, M.; Hill, S.; Goy, P.; Gross, M. *Rev. Sci. Instrum.* **2000**, *71*, 186.
- (22) Takahashi, S.; Edwards, R. S.; North, J. M.; Hill, S.; Dalal, N. S. *Phys. Rev. B* **2004**, *70*, 094429.
- (23) Hassan, A. K.; Pardi, L. A.; Krzystek, J.; Sienkiewicz, A.; Goy, P.; Rohrer, M.; Brunel, L. C. *J. Magn. Reson.* **2000**, *142*, 300.
- (24) Aromí, G.; Telsler, J.; Ozarowski, A.; Brunel, L.-C.; Stoeckli-Evans, H.-M.; Krzystek, J. *Inorg. Chem.* **2004**, *44*, 187.
- (25) Krzystek, J.; Ozarowski, A.; Telsler, J. *Coord. Chem. Rev.* **2006**, *250*, 2308.